ELECTROCHEMISTRY

Artificially steering electrocatalytic oxygen evolution reaction mechanism by regulating oxygen defect contents in perovskites

Min Lu[1]†, Yao Zheng[2]†, Yang Hu[1]†, Bolong Huang[3]*, Deguang Ji[1], Mingzi Sun[3], Jianyi Li[1], Yong Peng[4], Rui Si[5], Pinxian Xi[1]*, Chun-Hua Yan[1,6]

The regulation of mechanism on the electrocatalysis process with multiple reaction pathways is more efficient and essential than conventional material engineering for the enhancement of catalyst performance. Here, by using oxygen evolution reaction (OER) as a model, which has an adsorbate evolution mechanism (AEM) and a lattice oxygen oxidation mechanism (LOM), we demonstrate a general strategy for steering the two mechanisms on various $La_xSr_{1-x}CoO_{3-\delta}$. By delicately controlling the oxygen defect contents, the dominant OER mechanism on $La_xSr_{1-x}CoO_{3-\delta}$ can be arbitrarily transformed between AEM-LOM-AEM accompanied by a volcano-type activity variation trend. Experimental and computational evidence explicitly reveal that the phenomenon is due to the fact that the increased oxygen defects alter the lattice oxygen activity with a volcano-type trend and preserve the Co^0 state for preferably OER. Therefore, we achieve the co-optimization between the activity and stability of catalysts by altering the mechanism rather than a specific design of catalysts.

INTRODUCTION

The mechanistic understanding of the electrocatalytic oxygen evolution reaction (OER) in water electrolysis has rapidly developed in recent years (*1*–*6*). Previous studies proposed two major mechanisms including the traditional adsorbate evolution mechanism (AEM) and the recently proposed lattice oxygen oxidation mechanism (LOM). In the former mechanism, the transition metal ions serve as active centers and are coordinated with the reaction intermediates (e.g., *OOH and *OH) to form oxygen molecules. The latter one occurs on the lattice oxygen of oxides, which is governed by the intrinsic metal-oxygen covalency property of catalysts (*7*). A certain catalyst working in LOM shows much higher apparent activity in comparison with one working in AEM (*3*, *8*–*12*). However, many reports indicated that catalysts usually undergo a large extent of surficial reconstruction during the LOM process because of the redox and migration of lattice oxygen, which obviously decreases their stability. Conversely, catalysts usually present relatively high stability but low activity for the AEM process (*7*, *8*, *12*, *13*). Thus, the control of catalytic reaction pathway between AEM and LOM can realize the coordinated optimization between the activity and stability of the catalyst, which is crucial for the development of the next generation of highly efficient OER catalytic materials. However, the most dominant OER mechanism choice is realized by material engineering to achieve a unique electronic structure and the corresponding reaction intermediate's adsorption (*7*, *8*, *13*–*16*). For these methods, the dominant OER mechanism on a specific material is fixed (i.e., either AEM or LOM). It is still a challenge to realize the shift of AEM and LOM in a certain family of materials by keeping their chemical components unchanged (including element species and metal proportion) and only adjusting the defect content or introducing the lattice stress.The perovskite oxides have high structural tolerance, therefore allowing various element compositions and high defect contents (*17*, *18*). Such structural characteristics enable their band structures of metal 3d and oxygen 2p to be regulated in a wide range. Therefore, it is relatively reliable to regulate the dominant OER mechanism in perovskites compared to other oxides (*7*, *13*). For example, Shao-Horn, Stevenson, and Xu and their colleagues successfully realized either AEM or LOM in different perovskite oxides [e.g., $SrCoO_3$ as LOM and $LaCoO_3$ (LCO) as AEM] (*7*, *8*, *13*). However, there is still a lack of research on the regulation of OER mechanism in one family of materials with similar chemical properties and electronic structures. To achieve this target, a general activity descriptor is needed to correlate the physicochemical properties of materials with the reaction mechanism. In the past few decades, several OER activity descriptors have been developed, including e_g occupancy, d band center, lattice oxygen activity, and metal-oxygen covalency (*19*). In particular, the lattice oxygen activity can fundamentally guide whether the reaction mechanism is AEM or LOM in a range of catalysts (*7*, *8*). However, since these descriptors more physically correspond to the intrinsic electronic structure of the materials, the application of these descriptors in material design is limited (*19*). Oxygen defect content is one of the essential structural parameters in perovskites, which can be well characterized and easily regulated through controlled experiments (*20*–*22*). The content of oxygen defects can be correlated with the lattice oxygen activity of perovskites. This suggests that the oxygen defect may work as an activity descriptor to control the OER mechanism.

Following this consideration, here, we realize the OER mechanism steering (between AEM and LOM) in each group (with same

[1]State Key Laboratory of Applied Organic Chemistry, Frontiers Science Center for Rare Isotopes, College of Chemistry and Chemical Engineering, Lanzhou University, Lanzhou 730000, China. [2]School of Chemical Engineering and Advanced Materials, The University of Adelaide, Adelaide, South Australia 5005, Australia. [3]Department of Applied Biology and Chemical Technology, The Hong Kong Polytechnic University, Hung Hom, Kowloon, Hong Kong SAR, China. [4]School of Materials and Energy, Electron Microscopy Centre of Lanzhou University, Lanzhou 730000, China. [5]Shanghai Synchrotron Radiation Facility, Shanghai Institute of Applied Physics, Chinese Academy of Sciences, Shanghai 201204, China. [6]Beijing National Laboratory for Molecular Sciences, State Key Laboratory of Rare Earth Materials Chemistry and Applications, PKU-HKU Joint Laboratory in Rare Earth Materials and Bioinorganic Chemistry, College of Chemistry and Molecular Engineering, Peking University, Beijing 100871, China.
*Corresponding author. Email: bhuang@polyu.edu.hk (B.H.); xipx@lzu.edu.cn (P.X.)
†These authors contributed equally to this work.

La/Sr ratio) of $La_xSr_{1-x}CoO_{3-\delta}$ (LSCO) perovskites by only regulating its oxygen defect contents. We study the OER mechanism through four characterization methods, including ^{18}O labeling experiment, pH-dependent OER activity, electrochemical activation phenomenon, and in situ characterization of the reconstruction process; isotope labeling is the core method among them. Through the solid experimental evidence provided by the above characterizations, we succeeded in using the oxygen deficiency content as a descriptor and observing three catalytic mechanism shift models along with oxygen defect content change, including the OER mechanism shifts along the AEM-LOM, LOM-AEM, or AEM-LOM-AEM direction with the increase in oxygen defect contents in each group of LSCO. Besides, a volcano-type structure-function relationship between oxygen defect contents and OER activity has been observed under each specific OER mechanism (both AEM and LOM). Density functional theory (DFT) calculations unveil the cause of the above phenomenon: Co sites within the LSCO system experience a concentration lockup effect within increasing O vacancy (V_O) concentration. Further analysis demonstrates that the lattice relaxation response from nearest neighboring O_{NN} sites is strongly sensitive to the V_O concentration. The strong p-d coupling induces interionic pπ compensation, which simultaneously preserves the Co^0 state for the on-site oxidation activities by the localized O-2p tailband. The lattice oxygen activity also has a volcano-type trend with V_O concentration and only becomes active enough in appropriate concentration of oxygen defects and can directly participate in the OER process, which represents a LOM mechanism. We also show that this unique mechanism steering strategy can overcome an intrinsic activity limitation effect to enhance the OER activity in high oxygen defect concentration. Our work should contribute an important insight into the development of efficient catalysts by steering reaction mechanisms toward a multi-mechanism electrocatalytic process, which is more universal and practical than the current electronic structure design of catalysts.

RESULTS

Oxygen vacancy variations constructed by mechanical force

The pristine LSCO samples were prepared by the traditional sol-gel method. By regulating the atomic ratio between La and Sr (fig. S1 and table S1), we obtained a series of nonstoichiometric $La_xSr_{1-x}CoO_{3-\delta}$ ($0.05 \leq x \leq 1$) perovskites with different oxygen deficiencies (Fig. 1A and table S2). The energy-dispersive x-ray spectroscopy (EDS) elemental mappings indicate the uniform distributions of La, Sr, Co, and O atoms without phase segregation and separation (fig. S2). Taking $x = 0.5$ as an example (sample was hereby named LSCO-0.5), the high-angle annular dark-field image, annular bright-field (ABF) images, and atomic-resolution EDS mappings all (Fig. 1B and fig. S3) disclose a rhombohedral R-3c perovskite structure with $[11\bar{1}]$ orientation, which matched well with the XRD spectra (Fig. 1A). The oxygen vacancies were visualized by calculated relative O/Co intensity in the ABF image, showing an ordered spatial distribution of oxygen defects (Fig. 1C; see figs. S4 and S5 for details) (*13*, *23*). The valence states of Co atoms of all nine LSCO samples were investigated by x-ray absorption spectroscopy (XAS) to quantitatively characterize the concentration of oxygen defects (see fig. S6 and table S2 for details) (*24*–*28*). It is seen that the concentration of oxygen defects has a negative correlation with La substitution content (Fig. 1D), indicating the quantitative regulation of oxygen defects in LSCO.

We further used the mechanical force method to introduce lattice oxygen defects and create surface lattice termination in each initial LSCO material without the change of its composition (figs. S1 and S7 to S9). The concentration of oxygen defects has an approximate linear relationship with ball milling time (Fig. 1F and figs. S10 to S13). Detailed XRD analysis also shows an increased full width at half maximum of the (110) peak along with the ball milling time, demonstrating a decreased crystallinity and increased lattice defects (fig. S14). Co-local atomic structure analyzed by XAS indicates that the ball milling treatment did not change the perovskite-like structure of LSCO while altering the Co-O and Co-Co coordination structure (Fig. 1E and fig. S15) (*29*–*31*). Further fitting results of Fourier-transformed extended x-ray absorption fine structure (FT-EXAFS) show decreased Co-O coordination number (which matches well with oxygen defects change) and decreased Co-Co distance (Figs. 1, F and G, figs. S16 to S19, and tables S3 to S6). The negative shifted Co $L_{2,3}$-edge and positively shifted O K-edge spectra in the atomic-column resolution electron energy-loss spectroscopy (EELS; Fig. 1H and fig. S20) also support a decreased oxidation state of Co ions and an increased oxygen vacancy concentration along with the ball milling time (*32*, *33*), agreeing well with the EXAFS results. High-resolution transmission electron microscopy (HRTEM) and x-ray photoelectron spectroscopy (XPS) were also performed to study the surface structure of LSCO after ball milling (figs. S21 and S22). The results, including those of XRD and XAFS, indicated that the structure on the surface of materials remains in LSCO perovskite after 2 to 6 hours of ball milling. In addition, the variation trend of the oxygen defect content on the surface of the material is consistent with that in the bulk phase (δ) caused by ball milling.

Through the above study, we can find that both Sr substitution and ball milling treatment can lead to the formation of oxygen defects in LSCO. However, note that when the oxygen defect is introduced into the oxide without any other element's composition and proportion change, we can treat it as one type of material; these materials can be classified into a variety of its ideal structure composition. For example, $LaCoO_{3.02}$, $LaCoO_{2.95}$, and $LaCoO_{2.84}$ can be considered as LCO materials with different contents of oxygen defects.

When the oxygen defect of the material is realized by means of heterogeneous metal substitution or doping, such as $La_{0.25}Sr_{0.75}CoO_{2.72}$ and $La_{0.75}Sr_{0.25}CoO_{2.95}$, they should be regarded as two different materials: $La_{0.25}Sr_{0.75}CoO_3$ and $La_{0.75}Sr_{0.25}CoO_3$ with different contents of oxygen defects. As shown in fig. S23, the materials with different metal ratio (La/Sr ratio) also have diverse tolerance to oxygen defects. It not only results in individual intrinsic oxygen defect content in materials but also causes different oxygen defect contents in various materials under the same ball milling treatment. These results also make it difficult to study the relationship between oxygen defect and OER activity/mechanism. This is also one of the key points different from previous work in our research, which will be discussed in detail below.

The OER mechanisms in LSCOs

The alkaline OER performances on nine pristine LSCO before ball milling were first measured according to the cyclic voltammetry (CV) curves. LSCO-0.05 to LSCO-0.375 samples became more active after electrochemical activation, while LSCO-0.5 to LSCO-1 remained stable (Fig. 2A and fig. S24). This electrochemical activation phenomenon in the LSCO system was studied well in previous work (*9*–*11*). This activation of catalysts in LSCOs is usually accompanied

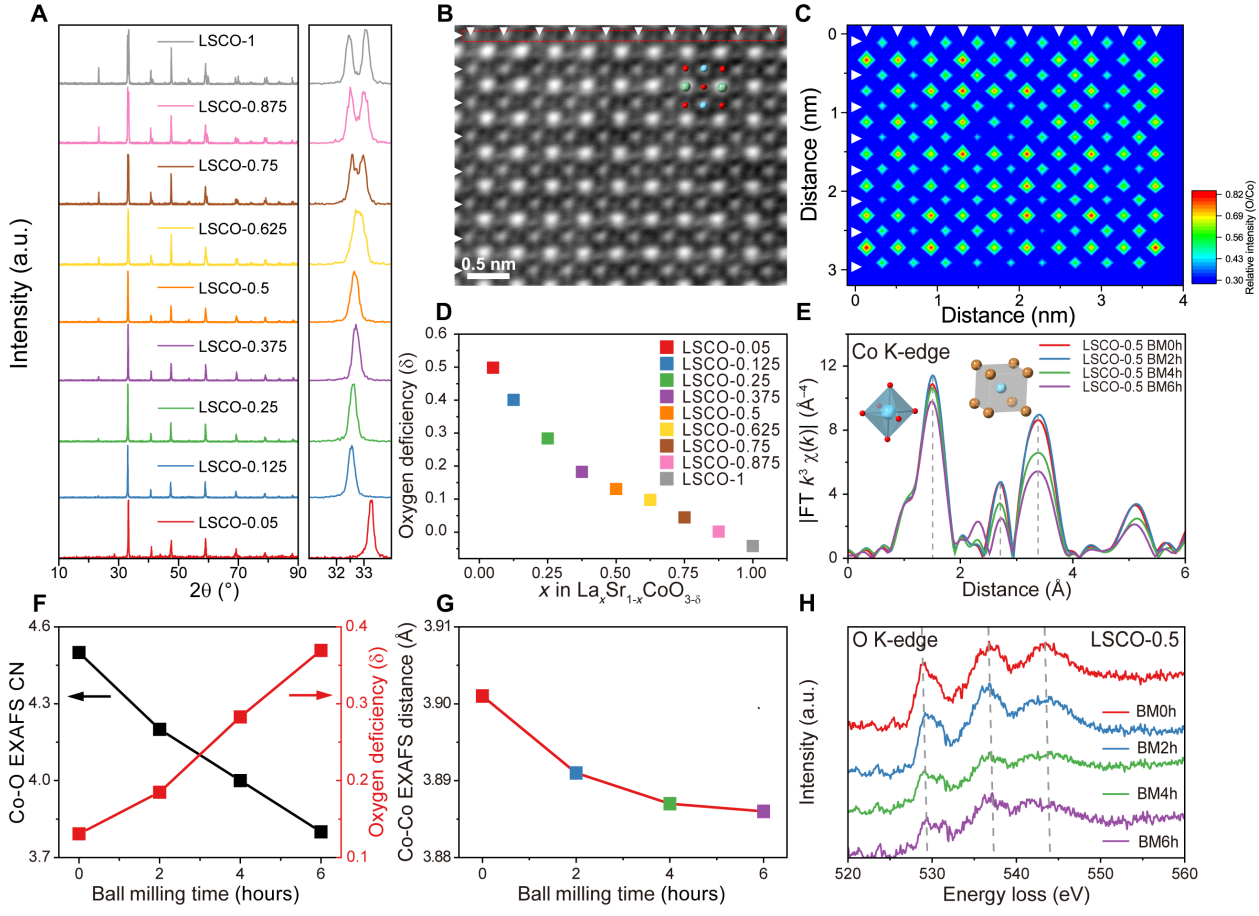

Fig. 1. Quantification and fine structure characterizations of oxygen defects in LSCOs. (**A**) XRD patterns before ball milling. a.u., arbitrary units. (**B**) ABF-STEM images of LSCO-0.5-0h. The arrangement of La, Sr, Co, and O atoms agrees with the LSCO perovskite structure. (**C**) Panel relative intensity analysis of O atoms in (B) consisting of every Co-O column and row (marked as white triangle). The oxygen defects present periodic content distribution on the two-dimensional projection plane (larger rhombus represents more oxygen defects). (**D**) Calculated oxygen deficiencies before ball milling. (**E**) FT-EXAFS $k^3\chi(k)$ spectra of LSCO-0.5. Three dominant peaks were observed at 1.4, 2.7, and 3.3 Å, corresponding Co-O, Co-La/Sr, and Co-Co single scattering, respectively. (**F**) Calculated oxygen deficiencies and fitted Co-O coordination number (CN) of LSCO-0.5 with different ball milling time. (**G**) Co-Co fitted EXAFS distance of LSCO-0.5 with different ball milling time. (**H**) O K-edge EELS spectra of LSCO-0.5 with different ball milling time.

by the dominant LOM mechanism due to the continuous activation of bulk lattice oxygen and its participation in the OER process as well as the local structure disordering during the LOM-OER of catalyst. This process is also usually accompanied by dynamic surface reconstruction (*7*, *8*, *13*). Shao-Horn and colleagues proposed that the activation degree is positively correlated with the thickness of the lattice oxygen atom in the material that participates in OER (*7*). In addition, the dominant OER mechanism of the above bulk LSCO materials has been demonstrated; specifically, when $x < 0.5$, samples exist in the LOM process and perform activity enhancement during the electrochemical activation process, and when $x \geq 0.5$, samples exist in the AEM process and also remain stable during OER (*13*).

After the controlled introduction of oxygen defects in a specific LSCO material by ball milling, taking LSCO-0.5 as an example, we further investigated the relationship between OER activity/mechanism and oxygen defect contents of specific materials with a fixed La/Sr ratio. LSCO-0.5-2h (LSCO-0.5 after 2 hours of ball milling treatment) and LSCO-0.5-4h showed 22.4 and 38.3% increased Brunauer-Emmett-Teller (BET)–normalized current density after electrochemical activation, respectively, and LSCO-0.5-0h and LSCO-0.5-6h remained almost stable (Fig. 2, B and C). To further verify the dominant OER mechanism of LSCO-0.5 with different oxygen defect contents, we conducted the pH-dependent OER activity test and in situ differential electrochemical mass spectroscopy (DEMS) measurements. The pH-dependent OER activity is typically exhibited in LOM (*7*, *8*, *34*, *35*). As seen in Fig. 2D, LSCO-0.5-2h and LSCO-0.5-4h show clear pH-dependent OER activity, while the other two do not. The DEMS measurements were also performed using the isotope ^{18}O-labeled catalysts to directly investigate the participation of lattice oxygen atoms in OER. As seen in Fig. 2E and fig. S25, LSCO-0.5-0h and LSCO-0.5-6h show almost no ^{18}O isotope in OER products, representing an AEM process, whereas LSCO-0.5-2h and LSCO-0.5-4h show 13.9 and 19.9% $^{34}O_2/^{32}O_2$ in products, respectively, representing a typical LOM process. The above results clearly reveal that the dominant OER mechanism of LSCO-0.5-0h and LSCO-0.5-6h can be assigned to AEM, while LSCO-0.5-2h and LSCO-0.5-4h are LOM. In other words, from 0 to 6 hours of ball milling, the dominant OER mechanism undergoes an AEM-LOM-AEM transformation on the LSCO-0.5 family of samples.

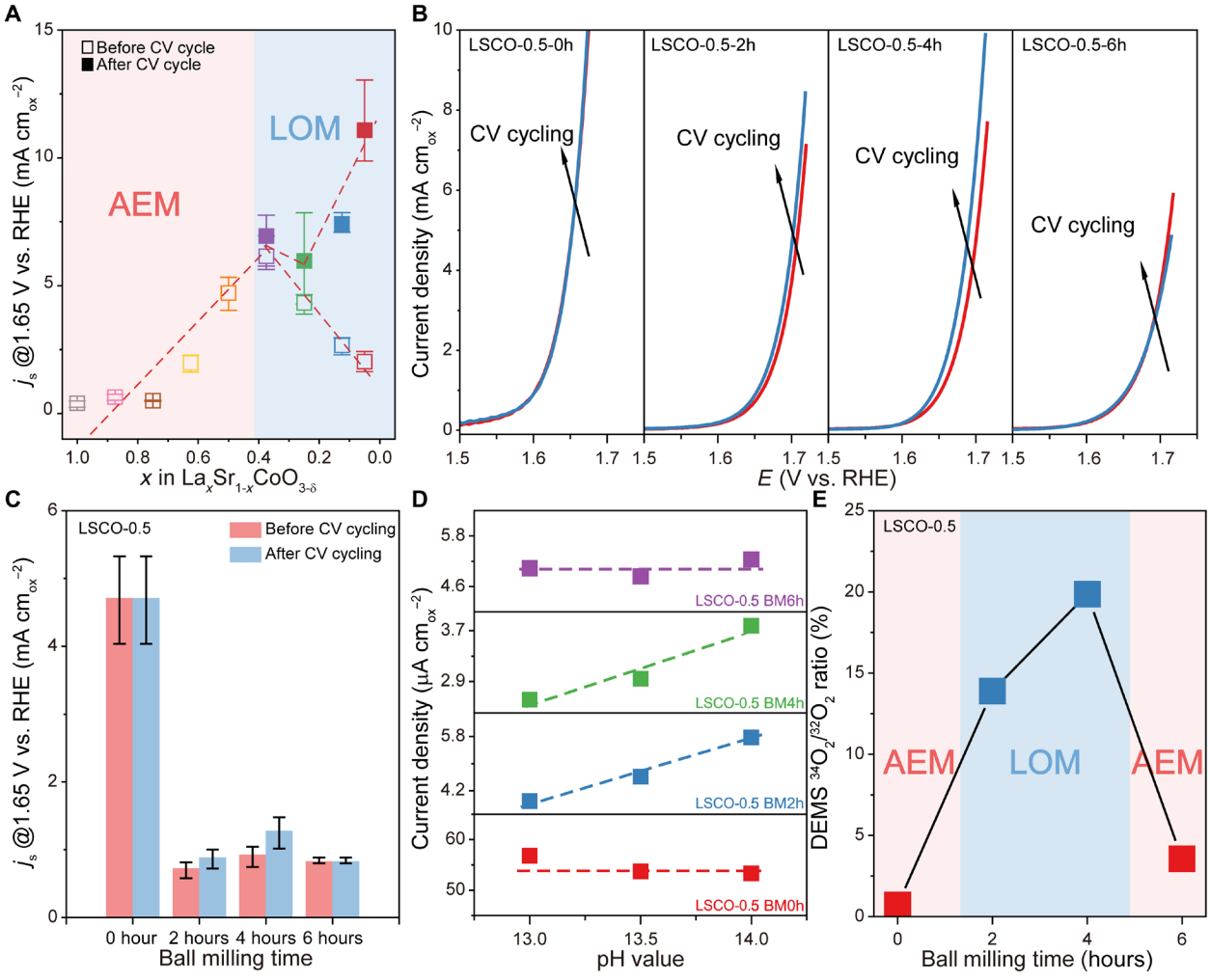

Fig. 2. OER performance of LSCOs. (**A**) Comparison of the normalized current densities based on oxide surface areas at 1.65 V versus RHE of LSCO-0h before (data were collected from the second CV curves) and after (data were collected from the best curves during cyclings) electrochemical activation. (**B**) Polarization curves of four LSCO-0.5 samples before and after electrochemical activation. (**C**) Comparison of the normalized current densities of LSCO-0.5 before and after ball milling. The error bars in (A) and (C) represent SD calculated from three parallel tests. (**D**) Current densities of four LSCO-0.5 samples as a function of the pH value. All the above current densities (j_s) were normalized by BET surface area. (**E**) DEMS signal ratios of $^{34}O_2$ ($^{16}O^{18}O$) and $^{32}O_2$ ($^{16}O^{16}O$) from the reaction products for ^{18}O-labeled LSCO-0.5 catalysts test in $H_2{}^{16}O$ aqueous KOH electrolyte.

The pH-dependent OER activity results and in situ DEMS results agree well with the electrochemical activation phenomenon and the activation degree in LSCO-0.5 (to eliminate test errors, all tests were run three times in parallel). Therefore, the existence of such activation phenomenon during CV processes can be used as an experimentally easily obtained qualitative basis to determine whether the catalytic mechanism is AEM or LOM in LSCO perovskites involved here. The shifting of the OER mechanism in LSCO materials is realized only through the change of the oxygen defect contents. With this criterion, the electrochemical measurements on all 36 LSCO samples with ball milling were then performed to study the relationship between oxygen defects and the OER mechanism.

Full picture of mechanism shifting

On the basis of the electrochemical measurement results (figs. S26 to S39), 36 materials can be divided into three categories according to the relationship between activation behavior and oxygen defects: LSCO-0.05 to LSCO-0.375, LSCO-0.5, and LSCO-0.625 to LSCO-0.75, which exhibit different mechanism shifting behaviors. For LSCO-0.05 to LSCO-0.375, with the introduction of oxygen defects by ball milling (from left to right for one sample), the OER activities' activation values of these four groups of materials decrease (Fig. 3A). According to the criteria, the dominant OER mechanism of LSCO-0.05-0h, LSCO-0.125-0h, LSCO-0.25-0h, and LSCO-0.375-0h is LOM due to their largest activation degree of OER activity increase in each group of samples. In addition, the introduction of oxygen defects inhibits the LOM activity and lastly shifts the dominant mechanism to AEM (all four 6-hour ball-milled samples show no activity increase). In brief, these four groups of materials experience a LOM to AEM (LOM-AEM) type of OER mechanism shift along with the oxygen defect increase. For LSCO-0.5, Fig. 3B indicates that LSCO-0.5-0h shows no activation after electrochemical activation, representing an AEM process. With the introduction of oxygen defects, the dominant mechanism shifts from AEM to LOM with the emergence of

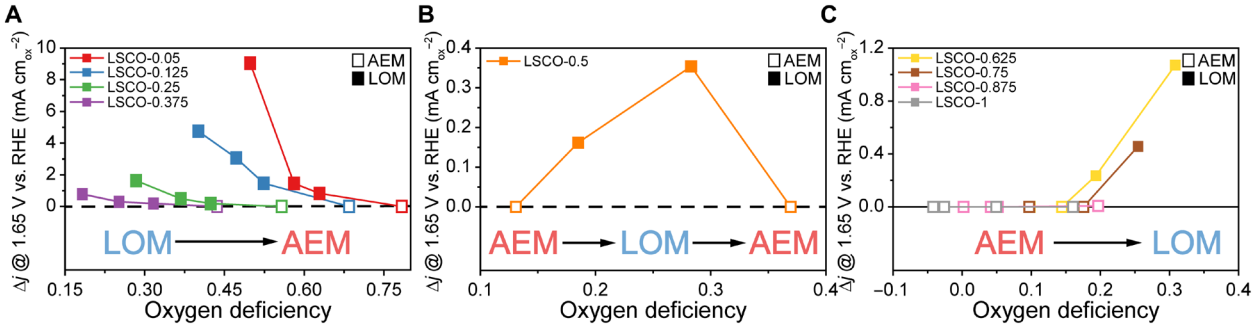

Fig. 3. OER mechanism shift patterns. (**A** to **C**) Three types of OER mechanism shift patterns observed from different materials. (A) LOM to AEM from LSCO-0.05 to LSCO-0.375, (B) AEM to LOM to AEM from LSCO-0.5, and (C) AEM to LOM from LSCO-0.625 to LSCO-0.75. Besides, LSCO-0.875 and LSCO-1 show no OER mechanism shift and remain AEM always. All data in the figure are the changed value of normalized current densities between second CV curves and best performance CV curves during electrochemical activation. For one sample with the same color code, from left to right represents an increase in oxygen defects and an increase in ball milling time.

electrochemical activation (LSCO-0.5-2h and LSCO-0.5-4h). As the oxygen defect continues to be introduced, the electrochemical activation of material disappears, representing the dominant mechanism shift to AEM again (LSCO-0.5-6h). In brief, LSCO-0.5 experiences an AEM-LOM-AEM type of mechanism shifting. For LSCO-0.625 to LSCO-0.75 (Fig. 3C), they have AEM-LOM shifting as oxygen defects increase. As to LSCO-0.875 and LSCO-1, they both show no electrochemical activation with total oxygen defect content range, indicating that the materials were always AEM.

On the basis of the above results, we show different mechanism change patterns such as AEM-LOM, LOM-AEM, and AEM-LOM-AEM with the increase in oxygen defects. A complete mechanism change pattern associated with oxygen defects should be that the dominant OER mechanism of the material undergoes an AEM-LOM-AEM change with the increase in oxygen defects. After ignoring the parameter La/Sr ratio, Fig. 4A establishes the relationship between OER activity/mechanism and oxygen defect for all 36 materials. It shows that LOM only exists at a moderate oxygen defect content; too much or too little oxygen defect shifts the process to AEM.

The OER mechanism shift pattern and the corresponding OER mechanism of each material discussed above provide an opportunity for us to understand the relationship between oxygen defect content and OER activity under a specific mechanism. As shown in figs. S38 and S39, for the AEM-OER, we can easily establish a volcano-type relationship between oxygen defect contents and OER activity through LSCO-0.875 and LSCO-1. The above two groups of materials always maintain AEM. However, for the LOM-OER, the situation becomes complicated. First, in the LOM region of the four groups of materials (LSCO-0.05 to LSCO-0.375), we observed that the OER activity decreased with the increase in oxygen defects, and lastly, the OER mechanism shifts from LOM to AEM. Second, in the LOM region of the three groups of materials (LSCO-0.5 to LSCO-0.75), we observed that OER activity increased with the increase in oxygen defect. Moreover, the OER mechanism shifts from AEM to LOM to AEM (LSCO-0.5) or AEM to LOM (LSCO-0.625 and LSCO-0.75) in these groups of materials. Considering the relationship between activity and oxygen defect contents in the LOM region as well as the mechanism shift pattern observed above, we can also obtain a volcano-type relationship between oxygen defect contents and OER activity.

To summarize, Fig. 4B illustrates that for an ideal perovskite oxide, with the increase of oxygen deficiency, the lattice oxygen activity was changed and led the dominant OER mechanism to undergo an AEM-LOM-AEM shifting pattern. For the earlier two mechanism regions (the first AEM and LOM), oxygen deficiency has a volcano-type trend with OER activity.

However, the overall oxygen defect content–OER activity–OER mechanism model proposed in Fig. 4B can only be observed in ideal perovskite oxides, and it is difficult to find in actual materials. This is because the chemical composition (element type and proportion) of materials notably affects their intrinsic structure. Therefore, there will be obvious differences in the intrinsic electronic structure and structural stability of various materials with different chemical composition. As shown in fig. S23, in the LSCO system, the change in La/Sr ratio will affect the intrinsic oxygen defect content of the material as well as the difficulty of oxygen defect regulation. This fact also limits the range of mechanism shift and activity changes that can be observed by regulating oxygen defects in a specific material.

The origin of mechanism shift

We used a series of LSCO-0.5 samples as a model, which shows the AEM-LOM-AEM shifting pattern, to study the physical origin of the mechanism shift caused by oxygen defects. DFT calculations were carried out to investigate the electronic structure change (Fig. 4, C to M). Within three typical modeling V_O concentrations (16.7% for Fig. 4C, 33.3% for Fig. 4D, and 50% for Fig. 4E), all active bonding and anti-bonding orbitals near the Fermi level (E_F) present strong p-d coupling at the nearby Co and ONN sites with varied spatial occupations (Fig. 4, C to E). By comparing the projected partial density of states (PDOSs), the Co-3d band not only plays a dominant role of strongly coupling with the O-2p band but also increases its own activities with Sr incorporation. The Co-3d bonding and anti-bonding orbital levels determine the predominant electronic transition nearby E_F in pristine LSCO. Meanwhile, La-4f orbitals contribute to the robust valence states of Co sites with varied V_O (Fig. 4F). Thus, it is insightful and necessary to focus on the Co-3d band from the site (Co-V_O-Co).

The PDOSs of the Co-3d band have been illustrated with different charge states (0, +2, and +3) at the V_O region, denoted as V_O^0, V_O^{2+}, V_O^{3+}, respectively (Fig. 4, G to I). Only at the V_O^0 state has the energetic interval of bonding and anti-bonding orbital level for the Co-3d band been narrowed and even toward metallic at a high concentration of 50% (Fig. 4G). In contrast, the intervals of Co-3d bands are evidently widened at both V_O^{2+} (Fig. 4H) and V_O^{3+} (Fig. 4I). Localized gap or tail states are induced by disorders of the second

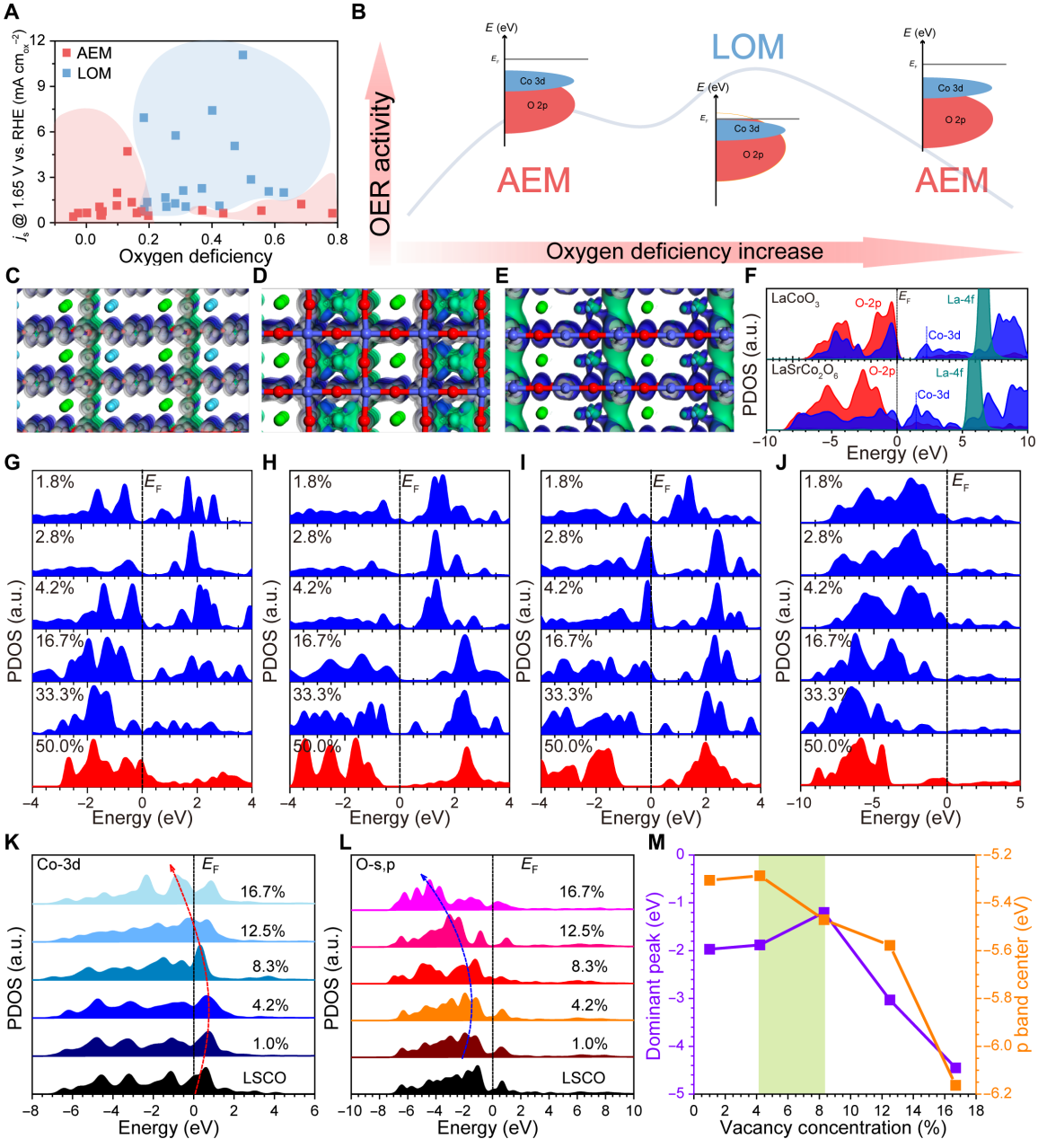

Fig. 4. The origin of OER mechanism shift. (**A**) Comparison of the normalized current densities and OER mechanism of all samples as a function of oxygen deficiency. (**B**) Illustration of mechanism shift and structure-activity relationship of OER controlled by oxygen defects. (**C** to **E**) The real spatial contour plots for bonding and anti-bonding orbitals near E_F regarding different V_O concentrations, such as for (C) 16.7%, (D) 33.3%, and (E) 50%; the red, blue, and green balls in (C) to (E) are O atoms, Co atoms, and La/Sr atoms, respectively. (**F**) PDOS comparison between LCO and $LaSrCo_2O_6$. (**G** to **I**) V_O concentration–dependent PDOSs of the Co-3d band at the (G) V_O^0 state, (H) V_O^{2+} state, and (I) V_O^{3+} state. (J) V_O concentration–dependent PDOSs of the nearest neighboring 2p band of O_{NN} at the V_O^0 state. (**K** and **L**) PDOS of Co-3d (K) and O-s,p. (L) in the $LaSrCo_2O_6$ model with varied V_O concentrations. (**M**) The dependence of dominant p band peaks and p band orbitals on the V_O concentration in a variety of $LaSrCo_2O_6$ models.

nearest neighboring O sites (O_{2NN}) and independent of the Co-3d band. The O-2p hostband and O-2p tailband are evidently distinguished with V_O concentration varied. Especially at the high concentration, the O-2p tailband shifts upward near E_F, showing a strong oxidizing character with the ultralow energetic barrier of electronic transitions (Fig. 4J). When the concentration of V_O shows shifting from the surface to the bulk, the PDOSs of Co-3d remain at a similar trend to the V_O^0 state, supporting the dependence of electroactivity on the V_O concentration (Fig. 4K). This indicates that the electron that transfers from the bulk to the surface imposes similar influences on the surface Co sites. Similarly, O-s,p orbitals of surface O sites also demonstrate an initial upshifting trend toward E_F and then downshift to a deeper position as the V_O concentration becomes higher, which further reveals the strong oxidizing feature (Fig. 4L). Detailed quantifications of the O-s,p clearly reflect the volcano trend in both dominant peak position and band center of the p band, supporting the experimental characterizations (Fig. 4M).

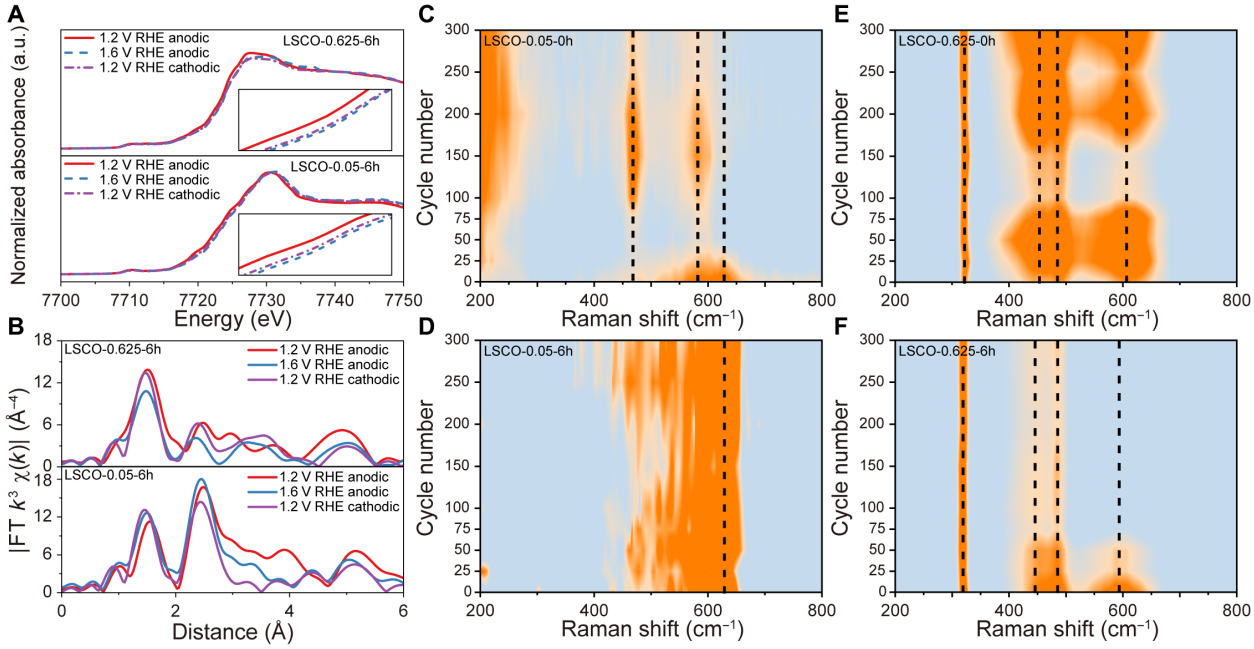

Fig. 5. Investigation of LSCO reconstruction behaviors during OER. (**A** and **B**) In situ (A) XANES and (B) EXAFS $k^3\chi(k)$ FT spectra of LSCO-0.05-6h and LSCO-0.625-6h samples under different potentials. (**C** to **F**) Different CV cycles' in situ Raman spectra of (C) LSCO-0.05-0h, (D) LSCO-0.05-6h, (E) LSCO-0.625-0h, and (F) LSCO-0.625-6h.

Specifically, the start material LSCO-0.5-0h has a relatively higher-valence cobalt and lower intrinsic oxygen defects compared with other samples (Fig. 1D and fig. S6), which leads to a relatively lower lattice oxygen activity and makes it perform an AEM. Then, the introduction of oxygen defects enhances the activity of lattice oxygen and drives it to participate directly in the OER process, therefore activating a LOM process. A further increase in the oxygen defect decreases the activity of lattice oxygen, which inhibits lattice oxygen participation in the reaction and triggers the AEM.

Validation of OER mechanism criterion by in situ spectroscopies

In addition to the electrochemical tests, we also used in situ XAS and Raman spectroscopies to characterize surface reconstruction to support our determination of the mechanism, because the LOM process is accompanied by the dynamic surface reconstruction during OER (*8*, *9*, *12*). In situ XAFS was performed to characterize the surface reconstruction of LSCO-0.05-6h and LSCO-0.625-6h, which shows AEM and LOM, respectively. Figure 5A shows an irreversible increase in the oxidation state of Co for both materials, which may be caused by the repair of oxygen deficiency at oxidizing OER conditions. Figure 5B reveals that the structure of LSCO-0.625-6h obviously changed at 1.6 V versus Reversible Hydrogen Electrode (RHE), and the structure of LSCO-0.05-6h remains nearly unchanged, agreeing well with electrochemical results. Raman spectra in different CV cycles (Fig. 5, C to F, and fig. S40) also support the XAS results. Specifically, the emergence of the new peak at ~466 (fig. S40A) and ~436 cm^{-1} (fig. S40D) and the weakening/disappearing peak at ~625 cm^{-1} (fig. S40A) and ~597 cm^{-1} (fig. S40D) are associated with the formation of CoOOH species, which indicates that LSCO-0.05-0h and LSCO-0.625-6h are working with LOM (*36*–*38*), while the unchanged spectra of LSCO-0.05-6h and LSCO-0.625-0h indicate the AEM mechanisms. Despite the fact that LOM is coupled with amorphization or surface reconstruction, this amorphization process is the dynamic structural evolution of the material in the catalytic process under the application of OER voltage. This evolution behavior and the OER mechanism of the material still depend on the original structure of the catalyst. Therefore, it is still reasonable and useful to use oxygen defect content as the structural parameter to describe the OER activity/mechanism of the catalyst. Co L-edge and O K-edge EELS spectra of LSCO0.5-0h also support the above results, in which the positive peak shift to higher energy indicates a more elevated Co valence state and lower oxygen deficiency of materials after OER (fig. S41).

The in-depth understanding of mechanism steering and activity variation caused by oxygen defects

In a full range of 36 samples, Fig. 6A displays the relationship between OER activity and oxygen defects. As we discussed earlier, OER activity has a volcano-type relationship with oxygen deficiencies both under AEM and LOM mechanisms. In addition, note that the OER activity of each group's samples shows a gradual decrease as the oxygen defects increase, in which the degree of the activity also decreases, which eventually stabilizes the activity. The increasing oxygen deficiency shows a limiting effect on OER activity. The above phenomenon is further studied by DFT calculation (Figs. 6, B to I).

Then, in-depth quantitative analysis shows that the O-2p tailband plays a key role in elevating the oxidation activities. With V_O concentration increased, the O-2p hostband offsets toward an even deeper range showing an inert character, while the O-2p tailband almost monotonically elevates the electronic activities by approaching the E_F. The green shaded area denotes that the strong oxidation activities have been preserved at the $V_O{}^0$ state (Fig. 6B). Then, the interionic distance variation analysis indicates that the unique Co^0 state arises from the pπ compensations of nearest neighboring O_{NN} site relaxations. The Co-Co distance is almost unchanged to lock up the Co^0 state, as the O_{NN}-O_{NN} vastly varies from attraction to repulsion for

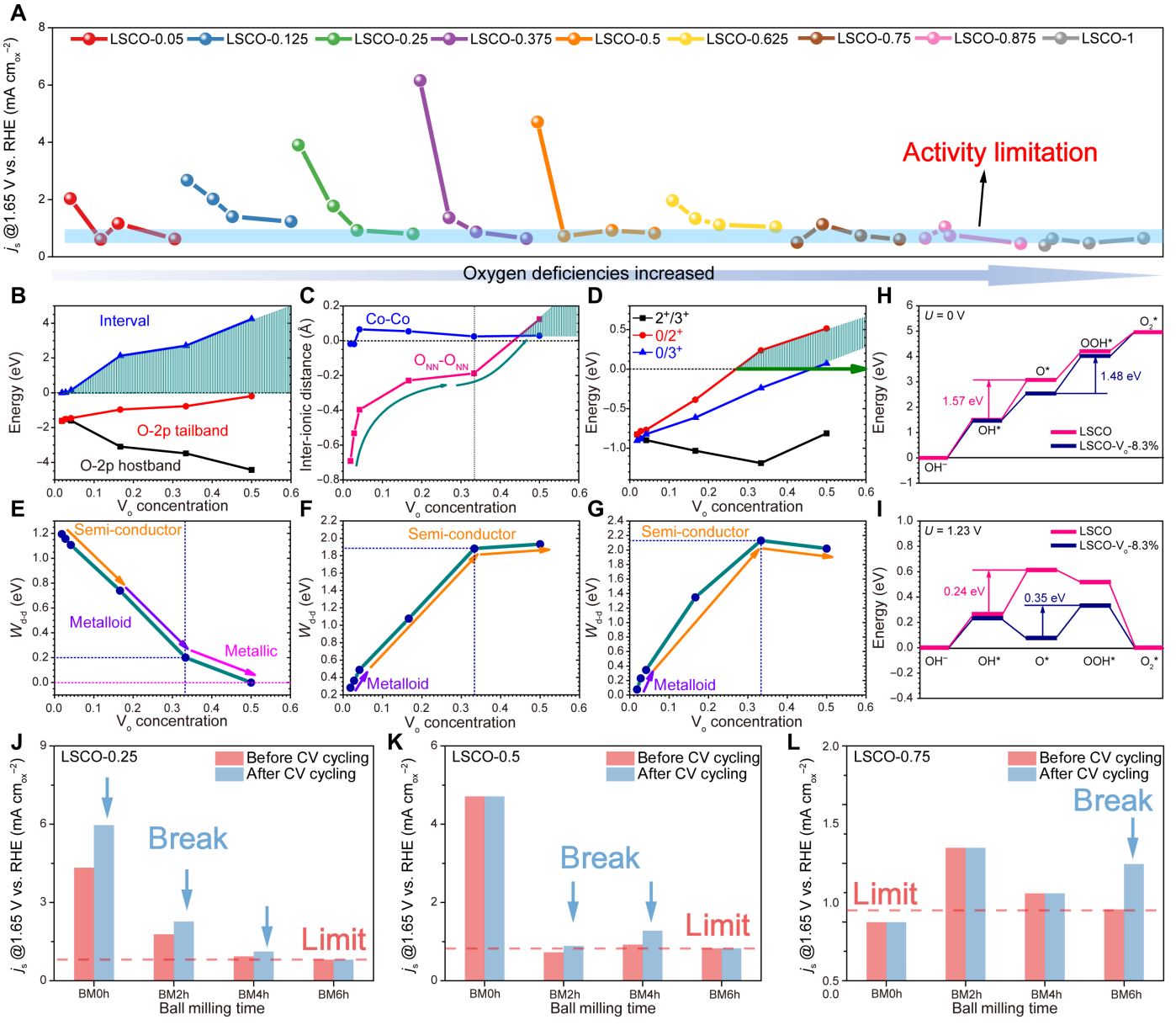

Fig. 6. The in-depth understanding of mechanism steering and activity variation caused by oxygen defects. (**A**) Comparison of the normalized current densities of all samples with different oxygen defect concentrations. The decreased stage of activity caused by increased oxygen deficiency clearly illustrated the intrinsic OER activity limitation effect. (**B**) Band offset variation behavior analysis of O-2p hostband, O-2p tailband, and their energetic intervals (green shaded area denotes the large preserved region for locking up the Co^0 state via pπ compensation). (**C**) The interionic distance variations of the Co^0 site near the V_O (Co-Co) and the nearest neighboring O site (O_{NN}-O_{NN}). (**D**) Behaviors of TTLs for the Co site among different charge transitions ($0/2^+$), ($0/3^+$), and ($2^+/3^+$), respectively. (**E** to **G**) The energetic interval between the HOMO and LUMO level ($W_{d\text{-}d}$) of the Co-3d orbital at the (E) V_O^0 state, (F) V_O^{2+} state, and (G) V_O^{3+} state. (**H** and **I**) The comparison of reaction energy of OER at (H) $U = 0$ and (I) 1.23 V. (**J** to **L**) Detailed intrinsic OER activity limitation and mechanism shift optimization analysis of (J) LSCO-0.25, (K) LSCO-0.5, and (L) LSCO-0.75. The separated bars from left to right in each figure represent increased ball milling time and oxygen defects.

neutralization (Fig. 6C). The thermodynamic transition level (TTL) analysis has also been interpreted as the charge-switching performance of the Co site given between different charge states. Indicated by the green shaded area, the difficulties of $0/2^+$ and $0/3^+$ transitions denote an evident uprising trend that potentially locks up the Co^0 state at high V_O concentrations (Fig. 6D). Further interorbital-based electronic transition ability for the Co (Co-V_O-Co) site has been directly reflected under three corresponding charge states (V_O^0, V_O^{2+}, and V_O^{3+}), respectively (Figs. 6, E to G). The $W_{d\text{-}d}$ denotes the energetic width between highest occupied molecular orbital (HOMO) and lowest unoccupied molecular orbital (LUMO) levels of Co-3d bands. We observe that the Co-3d orbital electronic transferability has been evidently shown in contrast. Under the neutral charge state (Co^0), the $W_{d\text{-}d}$ linearly narrows the gap width toward metallic with V_O concentration increased. In contrast, as long as the Co oxidation states are induced by either V_O^{2+} (Fig. 6F) or V_O^{3+} (Fig. 6G), the $W_{d\text{-}d}$ tends to

enlarge the gap widths toward the semi-conductor. To demonstrate the concentration lockup effect, we supplied a schematic diagram and corresponding discussions in fig. S42.

To evaluate the influences induced by the V_O on OER performances, we compared the reaction energy change. Notably, both LSCO and LSCO-V_O have delivered the uphill energy change trend, where the largest energy barrier is 1.57 and 1.48 eV, respectively, indicating the improved electroactivity (Fig. 6H). After applying the equilibrium potential of 1.23 V, the OER performance has been clearly distinguished. The lockup effect of V_O has led to a reduced overpotential of 250 mV, supporting the improved OER performance with increased V_O concentration (Fig. 6I). In addition, we supplied the reaction energy comparison with the LOM mechanism in fig. S43 (A and B). Notably, under 0 V, the rate-determining step of LOM shows an energy barrier of 1.74 eV, which is larger than that of AEM with 1.48 eV, supporting a high preference for the AEM at low V_O concentration (fig. S43, C and D). Therefore, with the comparison, our electronic structural analysis combined with the native point defect calculation simultaneously confirms that the Co^0 state has been preserved in both energetic preference and 3d orbital electronic transferability, with V_O concentration increased. This is also responsible for the volcano-type trend between OER activity and oxygen deficiency.

On the other hand, it was found that our mechanism steering method from AEM to LOM can overcome the intrinsic activity limitation on OER caused by oxygen defects found above, and eventually realizes the co-optimization between catalytic activity and stability. Figure. 6 (J and K) presents three groups of typical materials, LSCO-0.25, LSCO-0.5, and LSCO-0.75, with different dominant OER mechanisms to elaborate on this phenomenon. Figure 6J shows that the calculated activity descent rate (fig. S44) of LSCO-0.25 is −25.5, −15.1, and −0.9 mA cm^{-2}, respectively (with the oxygen defects increased). This significantly reduced amplitude of activity variation indicates that the lockup effect of oxygen defects on OER activity appeared and restricted OER activity. In addition, in LSCO-0.25, the dominant OER mechanism also shifts from LOM to AEM as the oxygen defect locks up the OER activity. Figure 6 (K and L) also indicates the existence of this lockup effect, especially in Fig. 6L. LSCO-0.75 with an AEM-LOM mechanism shift pattern shows an obvious lockup effect before electrochemical activation, and the decreasing degree of activity tended to be gentle with the increase in oxygen deficiency. However, the LSCO-0.75-6h with LOM shows an obviously increased activity after electrochemical activation and overcomes the limitation on OER activity. On the basis of this, we propose that the LOM mechanism can overcome the lockup effect because of the gradual activation of lattice oxygen in the bulk of materials during the catalytic process, which can directly participate in the OER process. The participation of bulk lattice oxygen extends the catalytic process from the surface to the bulk, dramatically expands the number of active sites, and improves the apparent catalytic activity (*7*). The above results prove that the controlling mechanism steering method overcomes the limitation of this lockup effect of oxygen defects on OER activity and can realize the coordinated optimization between material activity and stability.

DISCUSSION

We use OER as a model reaction to develop a comprehensive mechanism steering method in $La_xSr_{1-x}CoO_{3-\delta}$ perovskite. By quantitatively introducing oxygen defects into the specific material through finely controlled synthesis, we found three types of mechanism-shifting models including AEM-LOM, AEM-LOM-AEM, and LOM-AEM. DFT calculations reveal not only the origin of our mechanism steer methods by regulating oxygen defects but also that the lattice oxygen activity in LSCO system experiences a volcano-type trend. The LOM only exists in the appropriate oxygen defect concentration, in which the lattice oxygen is active enough to directly participate in the OER process. Further studies establish a comprehensive picture among OER activity, mechanisms, and oxygen defects in LSCO. The OER activity has a volcano-type relationship to oxygen defects under both AEM and LOM and experiences a limitation effect eventually at high oxygen defect concentration. A DFT study shows that V_O concentration increased and that the Co sites within the LSCO system experience a concentration lockup effect to pin the C_O^0, which usually not only presents a high catalytic activity but also experiences a high instability to be irreversibly oxidized into $Co^{2+/3+}$ easily, for fast reversible redox switching. It is essential for the on-site high oxidation activities for H_2O catalysis and caused the above volcano trend. Our mechanism steering method was also shown to be capable of overcoming the abovementioned limitation effect on OER activity and eventually realizing the coordinated optimization between material activity and stability. This work provides a inspiring strategy to coordinate catalysts' activity and stability in an electrocatalysis process with multiple reaction pathways by the regulation of reaction mechanisms.

MATERIALS AND METHODS

Chemicals

$La(NO_3)_3$, $Sr(NO_3)_2$, $Co(NO_3)_2$, EDTA, $NH_3{\cdot}H_2O$, citric acid, NaOH (99%), and KOH (99.99%) were purchased from InnoChem, Nafion perfluorinated resin solution in lower aliphatic alcohols and water (5 weight %) was purchased from Sigma-Aldrich, absolute ethanol and isopropanol were purchased from Aladdin, and deionized (DI) water was obtained from a Millipore auto-pure system (18.2 megohms; Millipore Ltd., USA). All other materials for electrochemical measurements were of analytical grade without further purification.

Synthesis of bulk $La_xSr_{1-x}CoO_{3-\delta}$

LSCO bulk powders were synthesized by using a sol-gel method according to stoichiometric amounts (molecular formula) of $La(NO_3)_3$, $Sr(NO_3)_2$, and $Co(NO_3)_2$. The above metal nitrates were dissolved in appropriate DI water under stirring until completely dissolved, and then EDTA (1.5 times the total molar amount of metal ions) was added to the solution under stirring, followed by adjusting the pH of the solution to 10 by the addition of aqueous NH_4OH. Citric acid (same with the total molar amount of metal ions) was then added into the solution, and the pH of the solution was adjusted to 10 by the addition of aqueous NH_4OH again. After a homogeneous solution is formed, the solution was heated to 95°C to form a gel, and then heated to 400°C to decompose into powder. Then, the powder is transferred to the corundum boat after cooling and calcined at 400°C for 4 hours at a heating rate of 2°C per minute in an oxygen atmosphere in a tubular furnace, then continued heating to 1100°C, and maintained at the same heating rate for 5 hours.

Ball milling treatment of bulk $La_xSr_{1-x}CoO_{3-\delta}$

The ball milling process was performed on an MSK-SFM-3 high-speed three-dimensional pendulum ball mill machine purchased

from Hefei Kejing Materials Technology Co. Ltd. One gram of LSCO bulk powder was mixed with Φ 6-mm agate ball and ethanol with a mass ratio of 1:6:0.79 in the Ar-filled glove box (O_2 concentration < 1 parts per million) and then sealed in an agate ball mill container. Then, ball milling was performed at a pendulum frequency of 1200 rpm for different times. For every 30 min of ball milling, the machine needed to stop for 30 min.

Physicochemical characterizations

XRD measurements were carried out on a Rigaku MiniFlex 600 diffractometer with Cu Kα radiation (λ = 0.1542 nm) from 10° to 80° under a constant voltage of 40 kV. The morphology and EDX elemental mappings of samples were analyzed using a Thermo Scientific Apreo S field emission scanning electron microscope at an acceleration voltage of 30 kV. Elemental mappings were performed on a Tecnai G2 F30 field-emission transmission electron microscope. Atomic-scale scanning TEM (STEM) images were recorded on a probe aberration-corrected STEM (FEI Cubed Themis Z, FEI, USA) operated at 300 kV. Inductively coupled plasma (ICP) optical emission spectrometry analyses were performed on a Plasma Quant PQ9000 ICP spectrometer. Synchrotron radiation XAFS spectroscopy at the Co K-edge was acquired in transmission mode by using a Si (111) double-crystal monochromator and Oxford ion chambers at the 1W1B station of the Beijing Synchrotron Radiation Facility. The XAFS test sample was coated on the tape from the powder samples after passing through a 400-mesh screen. The window function used in Fourier transforms is Hanning, the k range is 3 to 12, and the Fourier transform parameters in the fit are k_{min} = 2, k_{max} = 12, r_{min} = 1, and r_{max} = 4.5. The BET-specific surface area was determined by using N_2 sorption isotherm measurements at −196°C on Micromeritics TriStar 3020 equipment. In situ synchrotron radiation XAFS spectroscopy at the Co K-edge was acquired in transmission mode using a Si (111) double-crystal monochromator and Oxford ion chambers at the BL14W1 station of the Shanghai Synchrotron Radiation Facility operated at 3.5 GeV under "top-up" mode with a constant current of 220 mA. For the x-ray absorption near-edge structure (XANES) part, the experimental absorption coefficients as a function of energies μ(E) were processed by background subtraction and normalization procedures and reported as "normalized absorption" with E_0 = 7709 eV for all the measured samples and Co foil/Co_3O_4 standard. For the EXAFS part, the FT data in R space were used for comparison. In situ Raman spectroscopy measurements were conducted on a LabRAM HR Evolution spectrophotometer with a 532-nm wave number of the excitation light source. For in situ measurements, the powder sample was loaded on carbon paper and then inserted into an in situ cell for electrochemical measurements. For each voltage, the system was first stabilized for 5 min and then the XAFS test (15 min per point) or Raman test was started before the change of voltage.

Electrochemical measurements

All of the electrochemical measurements were conducted by using a CHI760E potentiostat in a typical three-electrode setup with O_2-saturated 1 M KOH solution. A Pt foil was used as the counter electrode, and Hg/HgO with 1 M KOH filling solution was used as the reference electrode. The as-measured potentials (versus Hg/HgO) were calibrated with respect to the RHE. A glassy carbon electrode with a diameter of 3 mm covered by a thin catalyst film was used as the working electrode. Typically, 5.6 mg of catalyst and 2.4 mg of acetylene black were suspended in 8 ml of isopropanol-water solution with a volume ratio of 4:1 to form a homogeneous solution assisted by ultrasound for 3 hours. Then, 0.95 ml of the as-prepared solution was mixed with 50 μl of Na^+-exchanged Nafion solution to form a homogeneous ink assisted by ultrasound for another 0.5 hours. The Na^+-exchanged Nafion solution was prepared by mixing commercial Nafion solution and 0.1 M NaOH solution with a volume ratio of 2:1 (*39*). Then, 2 μl of the ink was spread onto the surface of the glassy carbon electrode (mass loading: 0.028 mg cm^{-2}). The CV measurements were performed between 0.9254 and 1.7254 V_{RHE} (0 and 0.8 $V_{Hg/HgO}$) at 10 mV s^{-1}, the CV tests were carried out three times, and the mean and SD of the three test results were calculated (error bars). The upper and lower limits of the error bar represent the deviation degree of the maximum and minimum values in these three parallel data compared to the average values of these three data. The electrochemical activation process was performed with chronoamperometry between 1.0 and 1.7 V_{RHE} at a pulse width of 10 s (*29*). For every 50 cycles, a CV between 0.9254 and 1.7254 V_{RHE} (0 and 0.8 $V_{Hg/HgO}$) at 10 mV s^{-1} has been recorded. The potentials were corrected to compensate for the effect of solution resistance and calculated using the following equation: $E_{iR\ corrected} = E - iR$, where R is the uncompensated ohmic solution resistance measured via iR compensation module in CHI760E with a compensation level of 95%. All currents were normalized using a BET-specific surface area (fig. S45 and table S7).

DEMS measurements

DEMS measurements were carried out to determine the ^{18}O-labeled OER reaction products of LSCO-0.5 catalysts during the OER process using a QAS 100 device (Linglu Instruments, Shanghai). A saturated Ag/AgCl electrode and a Pt wire were used as the reference electrode and counter electrode, respectively. The working electrodes were prepared by sputtering Au onto a 50-μm-thick porous polytetrafluoroethylene films. Then, the catalysts were drop-cast onto the Au with a loading mass of 1 mg cm^{-2}. First, the catalysts were labeled with ^{18}O isotopes by performing 10 CV cycles at a scan rate of 10 mV/s in ^{18}O-labeled 1 M KOH solution between 0.2 and 0.8 $V_{Ag/AgCl}$. Afterward, ^{18}O-labeled electrodes were rinsed five times with ^{16}O water to remove the remaining $H_2{}^{18}O$. Last, the electrodes were subjected to CV cycles in ^{16}O 1 M KOH solution at the above potential window and scan rate. In the meantime, gas products of different molecular weights generated during the OER process were measured in real time by mass spectroscopy. Since catalysts were thoroughly rinsed with ^{16}O water after ^{18}O labeling, it is unlikely that ^{18}O species adsorbed on the surface contribute substantially to the observed $^{34}O_2$ ($^{16}O^{18}O$) signals. Thus, the participation of lattice oxygen from catalysts in OER can be determined by measuring the $^{34}O_2$ signals (*40*).

Calculation setup

Rotationally invariant DFT + U calculations (*41*) within CASTEP code (*42*) were performed. The Hubbard U parameters were self-consistently searched for La-4f, Co-3d, and O-2p orbitals with our two-way crossover linear response method (*43*), which was used for reflecting the electron-electron Coulomb potential for the transition metal ions with semi-core d orbitals (*43*–*50*). The algorithm of Broyden-Fletcher-Goldfarb-Shannon was chosen for all related ground-state geometry optimization, especially for interfacial relaxation. The cutoff energy of plane-wave basis sets for the total energy and valence electronic state calculations was set to 750 eV. The PBE

exchange-correlation functional was selected for DFT + U calculations. To improve the convergence quality of the transition metal compound system, the ensemble DFT method of Marzari *et al.* (*51*) was used during the electronic minimization process.

Regarding the LSCO model, the bulk lattice was built based on the relaxed cubic LCO, of which the bandgap width was 1.513 eV for LCO and $a = b = c = 3.828$ Å. The $LaSrCo_2O_6$ (LSCO) was built with 50% of La sites that were replaced by Sr sites, of which the minimum unit cell parameters were $a = b = 3.821$ Å and $c = 7.656$ Å. The supercell model was built with 180 atoms and a size of $4 \times 3 \times 3$, which is an appropriate size for V_O concentration calculations and avoids the edge effect. Within the lattice, $LaSrCo_2O_6$ includes 18 La atoms, 18 Sr atoms, 36 Co atoms, and 108 oxygen atoms, where the 50% V_O concentration corresponds to 54 empty O sites in the lattice. After geometry optimizations, the perovskite structure with different V_O concentrations from 1.0 to 50% remains stable. To alleviate the DFT computational demanding cost, the Monkhost-Pack reciprocal space integration was performed by using Gamma-center-off special k-points with mesh of $2 \times 2 \times 2$ (*52*), which was guided by the initial convergence test. With these settings, the overall total energy for each step was converged to less than 5.0×10^{-7} eV per atom. The Hellmann-Feynman forces on the atom were converged to less than 0.001 eV/Å. To deal with the charges in the V_O in the periodic lattice, a Coulomb potential correction is required to counteract the effects of the image charge of the crystal lattice. In this work, we applied the dipole correction developed by Makov and Payne (*53*), which considers the Madelung effect based on static electric Coulomb potential corrections.

The La, Sr, Co, and O norm-conserving pseudopotentials were generated by using the OPIUM code in the Kleinman-Bylander projector form (*54*), and the nonlinear partial core correction (*55*) and a scalar relativistic averaging scheme (*56*) were used to treat the mixed valence Co spin-orbital coupling effect. We chose the projector-based (4f, 5s, 5p, 5d, and 6s), (3d, 4s, and 4p), and (2s and 2p) states to reflect the valence states of La, Sr, Co, and O atoms, respectively. The Rappe-Rabe-Kaxiras-Joannopoulos (RRKJ) method was chosen for the optimization of the pseudopotentials (*57*). The Hubbard U parameters were self-consistently determined as $U_d = 3.06$ eV (Co-3d), $U_f = 2.21$ eV (La-4f), and $U_p = 7.37$ (O-2p).

SUPPLEMENTARY MATERIALS

Supplementary material for this article is available at https://science.org/doi/10.1126/sciadv.abq3563

REFERENCES AND NOTES

1. S. Chu, A. Majumdar, Opportunities and challenges for a sustainable energy future. *Nature* **488**, 294–303 (2012).
2. Z. W. She, J. Kibsgaard, C. F. Dickens, I. Chorkendorff, J. K. Nørskov, T. F. Jaramillo, Combining theory and experiment in electrocatalysis: Insights into materials design. *Science* **355**, eaad4998 (2017).
3. J. Suntivich, K. J. May, H. A. Gasteiger, J. B. Goodenough, Y. Shao-Horn, A perovskite oxide optimized for oxygen evolution catalysis from molecular orbital principles. *Science* **334**, 1383–1385 (2011).
4. J. Rossmeisl, Z.-W. Qu, H. Zhu, G.-J. Kores, J. K. Nørskov, Electrolysis of water on oxide surfaces. *J. Electroanal. Chem.* **607**, 83–89 (2007).
5. A. Li, S. Kong, C. Guo, H. Ooka, K. Adachi, D. Hashizume, Q. Jiang, H. Han, J. Xiao, R. Nakamura, Enhancing the stability of cobalt spinel oxide towards sustainable oxygen evolution in acid. *Nat. Catal.* **5**, 109–118 (2022).
6. H. Zhang, W. Zhou, J. Dong, X. F. Lu, X. W. Lou, Intramolecular electronic coupling in porous iron cobalt (oxy)phosphide nanoboxes enhances the electrocatalytic activity for oxygen evolution. *Energ. Environ. Sci.* **12**, 3348–3355 (2019).
7. A. Grimaud, O. Diaz-Morales, B. Han, W. T. Hong, Y.-L. Lee, L. Giordano, K. A. Stoerzinger, M. T. M. Koper, Y. Shao-Horn, Activating lattice oxygen redox reactions in metal oxides to catalyse oxygen evolution. *Nature. Chem.* **9**, 457–465 (2017).
8. Z.-F. Huang, J. Song, Y. Du, S. Xi, S. Dou, J. M. V. Nsanzimana, C. Wang, Z. J. Xu, X. Wang, Chemical and structural origin of lattice oxygen oxidation in Co-Zn oxyhydroxide oxygen evolution electrocatalysts. *Nat. Energy* **4**, 329–338 (2019).
9. T. Wu, S. Sun, J. Song, S. Xi, Y. Du, B. Chen, W. A. Sasangka, H. Liao, C. L. Gan, G. G. Scherer, L. Zeng, H. Wang, H. Li, A. Grimaud, Z. J. Xu, Iron-facilitated dynamic active-site generation on spinel $CoAl_2O_4$ with self-termination of surface reconstruction for water oxidation. *Nat. Catal.* **2**, 763–772 (2019).
10. Y. Duan, S. Sun, Y. Sun, S. Xi, X. Chi, Q. Zhang, X. Ren, J. Wang, S. J. H. Ong, Y. Du, L. Gu, A. Grimaud, Z. J. Xu, Mastering surface reconstruction of metastable spinel oxides for better water oxidation. *Adv.Mater.* **31**, 1807898 (2019).
11. Y. Zhou, S. Sun, J. Song, S. Xi, B. Chen, Y. Du, A. C. Fisher, F. Cheng, X. Wang, H. Zhang, Z. J. Xu, Enlarged Co-O covalency in octahedral sites leading to highly efficient spinel oxides for oxygen evolution reaction. *Adv.Mater.* **30**, 1802912 (2018).
12. J. Song, C. Wei, Z.-F. Huang, C. Liu, L. Zeng, X. Wang, Z. J. Xu, A review on fundamentals for designing oxygen evolution electrocatalysts. *Chem. Soc. Rev.* **49**, 2196–2214 (2020).
13. J. T. Mefford, X. Rong, A. M. Abakumov, W. G. Hardin, S. Dai, A. M. Kolpak, K. P. Johnston, K. J. Stevenson, Water electrolysis on $La_{1-x}Sr_xCoO_{3-\delta}$ perovskite electrocatalysts. *Nat. Commun.* **7**, 11053 (2016).
14. C. Wang, P. Zhai, M. Xia, Y. Wu, B. Zhang, Z. Li, L. Ran, J. Gao, X. Zhang, Z. Fan, L. Sun, J. Hou, Engineering lattice oxygen activation of iridium clusters stabilized on amorphous bimetal borides array for oxygen evolution reaction. *Angew. Chem. Int.* **133**, 27332–27340 (2021).
15. Y. Wen, P. Chen, L. Wang, S. Li, Z. Wang, J. Abed, X. Mao, Y. Min, C. T. Dinh, P. D. Luna, R. Huang, L. Zhang, L. Wang, L. Wang, R. J. Nielsen, H. Li, T. Zhuang, C. Ke, O. Voznyy, Y. Hu, Y. Li, W. A. Goddard III, B. Zhang, H. Peng, E. H. Sargent, Stabilizing highly active Ru sites by suppressing lattice oxygen participation in acidic water oxidation. *J. Am. Chem. Soc.* **143**, 6482–6490 (2021).
16. Z. Shi, Y. Wang, J. Li, X. Wang, Y. Wang, Y. Li, W. Xu, Z. Jiang, C. Liu, W. Xing, J. Ge, Confined Ir single sites with triggered lattice oxygen redox: Toward boosted and sustained water oxidation catalysis. *Joule.* **5**, 2164–2176 (2021).
17. J. Hwang, R. R. Rao, L. Giordano, Y. Katayama, Y. Yu, Y. Shao-Horn, Perovskites in catalysis and electrocatalysis. *Science* **358**, 751–756 (2017).
18. S. Stølen, E. Bakken, C. E. Mohna, Oxygen-deficient perovskites: Linking structure, energetics and ion transport. *Phys. Chem. Chem. Phys.* **8**, 429–447 (2006).
19. W. T. Hong, R. E. Welsch, Y. Shao-Horn, Descriptors of oxygen-evolution activity for oxides: A statistical evaluation. *J. Phys. Chem. C* **120**, 78–86 (2016).
20. K. Zhu, F. Shi, X. Zhu, W. Yang, The roles of oxygen vacancies in electrocatalytic oxygen evolution reaction. *Nano Energy* **73**, 104761 (2020).
21. Q. Ji, L. Bi, J. Zhang, H. Cao, X. S. Zhao, The role of oxygen vacancies of ABO_3 perovskite oxides in the oxygen reduction reaction. *Energ. Environ. Sci.* **13**, 1408–1428 (2020).
22. X. Zhang, X. Liu, Y. Zeng, Y. Tong, X. Lu, Oxygen defects in promoting the electrochemical performance of metal oxides for supercapacitors: Recent advances and challenges. *Small Methods* **4**, 1900823 (2020).
23. D. Ávila-Brande, G. King, E. Urones-Garrote, Subakti, A. Llobet, S. García-Martín, Structural determination and imaging of charge ordering and oxygen vacancies of the multifunctional oxides $REBaMn_2O_{6-\chi}$ (RE = Gd, Tb). *Adv. Funct. Mater.* **24**, 2510–2517 (2014).
24. J. Yin, J. Jin, H. Liu, B. Huang, M. Lu, J. Li, H. Liu, H. Zhang, Y. Peng, P. Xi, C.-H. Yan, $NiCo_2O_4$-based nanosheets with uniform 4 nm mesopores for excellent Zn-air battery performance. *Adv. Mater.* **32**, 2001651 (2020).
25. C. Wei, Z. Feng, G. G. Scherer, J. Barber, Y. Shao-Horn, Z. J. Xu, Cations in octahedral sites: A descriptor for oxygen electrocatalysis on transition-metal spinels. *Adv. Mater.* **29**, 1606800 (2017).
26. Y. Zhou, S. Sun, S. Xi, Y. Duan, T. Sritharan, Y. Du, Z. J. Xu, Superexchange effects on oxygen reduction activity of edge-sharing $[Co_xMn_{1-x}O_6]$ octahedra in spinel oxide. *Adv. Mater.* **30**, 1705407 (2018).
27. K. Conder, E. Pomjakushina, A. Soldatov, E. Mitberg, Oxygen content determination in perovskite-type cobaltates. *Mater. Res. Bull.* **40**, 257–263 (2005).
28. J. Mastin, M.-A. Einarsrud, T. Grande, Structural and thermal properties of $La_{1-x}Sr_xCoO_{3-\delta}$. *Chem. Mater.* **18**, 6047–6053 (2006).
29. E. Fabbri, M. Nachtegaal, T. Binninger, X. Cheng, B.-J. Kim, J. Durst, F. Bozza, T. Graule, R. Schäublin, L. Wiles, M. Pertoso, N. Danilovic, K. E. Ayers, T. J. Schmidt, Dynamic surface self-reconstruction is the key of highly active perovskite nano-electrocatalysts for water splitting. *Nat. Mater.* **16**, 925–931 (2017).
30. T. C. Gibb, Evidence for an unusual phase in the perovskite-related system BaCoxMn1-xO3-y from EXAFS spectroscopy. *J. Mater. Chem.* **2**, 387–393 (1992).

31. M. Risch, A. Grimaud, K. J. May, K. A. Stoerzinger, T. J. Chen, A. N. Mansour, Y. Shao-Horn, Structural changes of cobalt-based perovskites upon water oxidation investigated by EXAFS. *J. Phys. Chem. C* **117**, 8628–8635 (2013).
32. T.-H. Shen, L. Spillane, J. Vavra, T. H. M. Pham, J. Peng, Y. Shao-Horn, V. Tileli, Oxygen evolution reaction in $Ba_{0.5}Sr_{0.5}Co_{0.8}Fe_{0.2}O_{3-\delta}$ aided by intrinsic Co/Fe spinel-like surface. *J. Am. Chem. Soc.* **142**, 15876–15883 (2020).
33. X. Zeng, J. Zhang, M. Si, D. Cao, X. Deng, H. Ma, Q. Lan, D. Xue, X. Zhang, K. Tao, Y. Peng, Direct imaging of dopant sites in rare-earth element-doped permanent magnet and correlated magnetism origin. *Nanoscale* **11**, 4385–4393 (2019).
34. L. Giordano, B. Han, M. Risch, W. T. Hong, R. R. Rao, K. A. Stoerzinger, Y. Shao-Horn, pH dependence of OER activity of oxides: Current and future perspectives. *Catal. Today* **262**, 2–10 (2016).
35. P. Zhang, L. Li, D. Nordlund, H. Chen, L. Fan, B. Zhang, X. Sheng, Q. Daniel, L. Sun, Dendritic core-shell nickel-iron-copper metal/metal oxide electrode for efficient electrocatalytic water oxidation. *Nat. Commun.* **9**, 381 (2018).
36. S. Zuo, Z. P. Wu, H. Zhang, X. W. Lou, Operando monitoring and deciphering the structural evolution in oxygen evolution electrocatalysis. *Adv. Energy Mater.* **12**, 2103383 (2022).
37. J. A. Koza, C. M. Hull, Y. -C. Liu, J. A. Switzer, Deposition of β-$Co(OH)_2$ films by electrochemical reduction of tris(ethylenediamine)cobalt(III) in alkaline solution. *Chem. Mater.* **25**, 1922–1926 (2013).
38. X. Bo, Y. Li, X. Chen, C. Zhao, Operando Raman spectroscopy reveals Cr-induced-phase reconstruction of NiFe and CoFe oxyhydroxides for enhanced electrocatalytic water oxidation. *Chem. Mater.* **32**, 4303–4311 (2020).
39. J. Suntivich, H. A. Gasteiger, N. Yabuuchi, Y. Shao-Horn, Electrocatalytic measurement methodology of oxide catalysts using a thin-film rotating disk electrode. *J. Electrochem. Soc.* **157**, B1263–B1268 (2010).
40. J. F. de Araffljo, F. Dionigi, T. Merzdorf, H. -S. Oh, P. Strasser, Evidence of Mars-Van-Krevelen mechanism in the electrochemical oxygen evolution on Ni-based catalysts. *Angew. Chem. Int. Ed. Engl.* **60**, 14981–14988 (2021).
41. I. A. Vladimir, F. Aryasetiawan, A. I. Lichtenstein, First-principles calculations of the electronic structure and spectra of strongly correlated systems: The LDA+U method. *J. Phys. Condens. Matter* **9**, 767–808 (1997).
42. S. J. Clark, M. D. Segall, C. J. Pickard, P. J. Hasnip, M. I. J. Probert, K. Refson, M. C. Payne, First principles methods using CASTEP. *Z. Kristallogr. Krist.* **220**, 567–570 (2005).
43. B. Huang, 4f fine-structure levels as the dominant error in the electronic structures of binary lanthanide oxides. *J. Comput. Chem.* **37**, 825–835 (2016).
44. B. Huang, R. Gillen, J. Robertson, Study of CeO_2 and its native defects by density functional theory with repulsive potential. *J. Phys. Chem. C* **118**, 24248–24256 (2014).
45. B. Huang, Superiority of DFT+U with non-linear core correction for open-shell binary rare-earth metal oxides: A case study of native point defects in cerium oxides. *Philos. Mag.* **94**, 3052–3071 (2014).
46. B. Huang, Intrinsic deep hole trap levels in Cu_2O with self-consistent repulsive Coulomb energy. *Solid State Commun.* **230**, 49–53 (2016).
47. B. Huang, Strong compensation hinders the p-type doping of ZnO: A glance over surface defect levels. *Solid State Commun.* **237-238**, 34–37 (2016).
48. B. Huang, Unraveling energy conversion modeling in the intrinsic persistent upconverted luminescence of solids: A study of native point defects in antiferromagnetic Er_2O_3. *Phys. Chem. Chem. Phys.* **18**, 13564–13582 (2016).
49. B. Huang, The screened pseudo-charge repulsive potential in perturbed orbitals for band calculations by DFT+U. *Phys. Chem. Chem. Phys.* **19**, 8008–8025 (2017).
50. J. Hu, B. Huang, C. Zhang, Z. Wang, Y. An, D. Zhou, H. Lin, M. K. H. Leung, S. Yang, Engineering stepped edge surface structures of MoS_2 sheet stacks to accelerate the hydrogen evolution reaction. *Energ. Environ. Sci.* **10**, 593–603 (2017).
51. N. Marzari, D. Vanderbilt, M. C. Payne, Ensemble density-functional theory for *ab initio* molecular dynamics of metals and finite-temperature insulators. *Phys. Rev. Lett.* **79**, 1337–1340 (1997).
52. M. I. J. Probert, M. C. Payne, Improving the convergence of defect calculations in supercells: An *ab initio* study of the neutral silicon vacancy. *Phys. Rev. B* **67**, 075204 (2003).
53. G. Makov, M. C. Payne, Periodic boundary conditions in *ab initio* calculations. *Phys. Rev. B. Condens. Matter* **51**, 4014–4022 (1995).
54. L. Kleinman, D. M. Bylander, Efficacious form for model pseudopotentials. *Phys. Rev. Lett.* **48**, 1425–1428 (1982).
55. S. G. Louie, S. Froyen, M. L. Cohen, Nonlinear ionic pseudopotentials in spin-density-functional calculations. *Phys. Rev. B* **26**, 1738–1742 (1982).
56. I. Grinberg, N. J. Ramer, A. M. Rappe, Transferable relativistic Dirac-Slater pseudopotentials. *Phys. Rev. B* **62**, 2311–2314 (2000).
57. A. M. Rappe, K. M. Rabe, E. Kaxiras, J. D. Joannopoulos, Optimized pseudopotentials. *Phys. Rev. B* **41**, 1227–1230 (1990).
58. A. L. Garay, A. Pichona, S. L. James, Solvent-free synthesis of metal complexes. *Chem. Soc. Rev.* **36**, 846–855 (2007).
59. K. Kubota, H. Ito, Mechanochemical cross-coupling reactions. *Trends Chem.* **2**, 1066–1081 (2020).
60. S. L. James, C. J. Adams, C. Bolm, D. Braga, P. Collier, T. Friščić, F. Grepioni, K. D. M. Harris, G. Hyett, W. Jones, A. Krebs, J. Mack, L. Maini, A. G. Orpen, I. P. Parkin, W. C. Shearouse, J. W. Steedk, D. C. Waddelli, Mechanochemistry: Opportunities for new and cleaner synthesis. *Chem. Soc. Rev.* **41**, 413–447 (2012).
61. P. G. Fox, Mechanically initiated chemical reactions in solids. *J. Mater. Sci.* **10**, 340–360 (1975).

Acknowledgments: We thank the 1W1B station of the Beijing Synchrotron Radiation Facility (BSRF) and the BL14W1 station of Shanghai Synchrotron Radiation Facility (SSRF) for supporting the XAFS measurements. **Funding:** This work was funded by the National Key R&D Program of China (2021YFA1501101), the National Natural Science Foundation of China (NSFC; nos. 21922105 and 21931001), the Special Fund Project of Guiding Scientific and Technological Innovation Development of Gansu Province (2019ZX-04), and the 111 Project (B20027). We also acknowledge support by the Fundamental Research Funds for the Central Universities (lzujbky-2021-pd04, lzujbky-2021-it12, and lzujbky-2021-37). B.H. acknowledges the support of the NSFC (no. 21771156), the NSFC/RGC Joint Research Scheme (N_PolyU502/21), and the funding for Projects of Strategic Importance of The Hong Kong Polytechnic University (project code: 1-ZE2V). Y.Z. acknowledges funding from the Australian Research Council (DP190103472 and FT200100062). **Author contributions:** M.L., P.X., Y.Z., and C.-H.Y. conceived the original concept and initiated the project. M.L. prepared the materials; performed the electrochemical and XRD and Raman measurements; and analyzed electrochemical, XAS, Raman, and XPS data. D.J. performed electrochemical and XRD measurements. R.S. helped design the setup for in situ XAS measurements. J.L. and M.L. carried out the in situ XAS measurements. B.H. and M.S. worked on the DFT calculations and analysis. Y.H. and Y.P. carried out TEM and STEM-EELS investigations. M.L. and Y.H. analyzed the TEM and EELS data. M.L. wrote the manuscript with input from all authors. Y.H. wrote the manuscript with input from TEM and STEM-EELS investigations. Y.Z. revised the manuscript with input from M.L. and Y.H. All authors have contributed to the revisions of the manuscript. **Competing interests:** The authors declare that they have no competing interests. **Data and materials availability:** All data needed to evaluate the conclusions in the paper are present in the paper and/or the Supplementary Materials.

Submitted 3 April 2022
Accepted 15 June 2022
Published 29 July 2022
10.1126/sciadv.abq3563